Single-molecule analysis of protein targeting from the endoplasmic reticulum to lipid droplets

Arda Mizrak [1], Jacob Kæstel-Hansen [2], Jessica Matthias[3], J. Wade Harper [1], Nikos S. Hatzakis [2,4], Tobias C. Walther [5,6,*], Robert V. Farese Jr. [5 *]

[1] *Department of Cell Biology, Harvard Medical School, Boston, MA, USA*
[2] *Department of Chemistry & Nanoscience Center, University of Copenhagen, Copenhagen, Denmark*
[3] *Abberior Instruments America, Bethesda, MD, USA*
[4] *Novo Nordisk Center for Optimised Oligo Escape and Control of Disease, University of Copenhagen, Copenhagen, Denmark*
[5] *Cell Biology Program, Sloan Kettering Institute, Memorial Sloan Kettering Cancer Center, New York, NY, USA*
[6] *Howard Hughes Medical Institute, NY, USA*

** Contributed equally.*

Corresponding authors: Tobias Walther (twalther@mskcc.org) and Robert Farese Jr. (rfarese@mskcc.org)

Highlights

- Single-molecule tracking reveals the path of ER-to-LD trafficking
- Cargo diffuses with similar speeds in both organelles
- Protein accumulating on LDs exhibits more confined motion on the LD surface
- Cargo moves bidirectionally between ER and LDs via seipin-mediated membrane bridges

SUMMARY

Numerous proteins migrate from the bilayer membrane of the endoplasmic reticulum (ER) to the monolayer surface of lipid droplets (LD) to perform critical metabolic functions. How cargoes move between these organelles and accumulate on LDs is unclear, particularly for mammalian cells. Here, we developed a synchronized ER-to-LD protein-trafficking assay and combined it with MINFLUX- and HILO-based single-molecule tracking and machine-learning analysis. Trafficking of a model protein *LiveDrop* between the ER and LDs occurs by diffusion through seipin-associated ER-LD membrane bridges that allow bidirectional protein movement. Unexpectedly, *LiveDrop* moves with the same apparent diffusion coefficient in the ER and LDs, but becomes molecularly confined at LD surfaces through a mechanism requiring its tryptophan residues. These data show how a specific LD-targeting membrane sequence leads to confined motion and LD protein accumulation, and directly demonstrate intra-organellar protein trafficking through membrane contact sites.

Key words: protein targeting, lipid droplet, endoplasmic reticulum, LiveDrop, seipin, RUSH, single-molecule tracking, MINFLUX, machine-learning, membrane bridge

INTRODUCTION

How cellular organelles achieve their protein composition is a fundamental question. For some organelles, such as the endoplasmic reticulum (ER) or mitochondria, dedicated protein machinery facilitates protein import. Other organelles have membranes that contain specific lipids, such as phosphoinositides, that direct proteins to the membrane. However, the mechanisms by which proteins target to and accumulate at lipid droplets (LDs) remain poorly understood.

LDs are unusual organelles composed of an organic oil phase, containing neutral lipids such as triacylglycerols (TGs) or cholesterol esters (CEs). These lipids serve as a reservoir of metabolic energy and precursors of membrane lipids. Unlike other organelles, LDs are bounded by a monolayer of phospholipids that harbors a distinct set of embedded proteins. LD-associated proteins include crucial metabolic enzymes, such as the lipid synthesis enzyme GPAT4 and the TG lipase ATGL. Mutations in several human LD proteins (e.g., PNPLA3, ATGL, CCTa, HSD17B13) alter their localization or accumulation on LDs and are linked to metabolic diseases (BasuRay et al., 2019; Ma et al., 2019; Olzmann et al., 2013; Zimmermann et al., 2004)

Most proteins reach the LD surface from the cytosol or the ER. Proteins targeting LDs from the cytosol bind to the monolayer surface at phospholipid packing defects, often using sequences that fold into amphipathic helices (Chorlay & Thiam, 2020; Čopič et al., 2018; Kim & Swanson, 2020; Prévost et al., 2018; Rowe et al., 2016). For the ER-to-LD targeting pathway, important for enzymes such as GPAT4 and HSD17B13, many questions remain. Typically, cargoes of this pathway contain hydrophobic hairpin domains inserted into the ER membrane during their synthesis. A current model posits that these proteins traffic to LDs through ER-LD membrane bridges (Olarte et al., 2020; Salo et al., 2016; Song et al., 2022; Wilfling et al., 2013). In *Drosophila* cells, some proteins using this pathway appear to target LDs as they form at LD assembly complexes (LDACs), composed of seipin and LDAF1 oligomers. For instance, the model cargo *LiveDrop,* containing a hydrophobic segment of GPAT4, appears to accumulate on LDs as they form (Olarte et al., 2020; Wilfling et al., 2013). However, other proteins, such as full-length GPAT4, target to LDs after their initial formation, via a process requiring machinery typically involved in secretory cargo exit from the ER, such as ER exit sites (ERES), or COPII and membrane fusion proteins (Song et al., 2022; Wilfling et al., 2014) .

How molecules move from the ER to LDs has been investigated less in mammalian cells. One challenge in analyzing these pathways in these cells is that the movement of proteins from the ER to LDs is a rare event that is difficult to capture with conventional microscopy analysis. Additionally, transport occurs within a densely populated ER membrane network that maintains contact sites with LDs and other organelles, making it difficult to resolve the trafficking routes with conventional fluorescence microscopy. Often, it is challenging even to determine whether molecules are located on the LD surface or within the closely associated ER network.

Also unclear is how some LD proteins initially inserted into the ER accumulate at LDs, rather than equilibrating between the two compartments. In *Drosophila* cells, tryptophan and positively changed residues within the hydrophobic segment of the model cargo *LiveDrop* (derived from GPAT4) are important for its accumulation at LDs. Molecular dynamics (MD) simulations suggested this cargo adopts a lower free energy conformation on the monolayer surface than the ER (Olarte et al., 2020), providing a possible thermodynamic explanation for its accumulation at LDs. However, alternative models, such as a trapping mechanism on LDs or selective degradation of proteins in the ER (Reggiano et al., 2016), also remain possible.

Here, we sought to overcome the challenges in studying ER-to-LD targeting by engineering a system for temporal control and measurement of protein transport at single-molecule resolution in live human cells. We developed a synchronized ER-to-LD protein-transport assay with modified retention using specific hooks (RUSH) methodology (Boncompain et al., 2012) and combined it with single-molecule tracking and a deep learning–based analysis pipeline, DeepSPT (Kæstel-Hansen et al., 2023), to detect and analyze rare ER-to-LD transitions as

proteins move between these compartments. This model system allowed us to study the ER-to-LD-targeting behavior of a model protein, *LiveDrop*, with unprecedented temporal and spatial resolution.

RESULTS

Synchronized cargo release reveals that all LDs are connected to the ER and can receive a model ER cargo

To analyze ER-to-LD targeting synchronously, we developed a method to uncouple insertion of proteins into the ER from their transport onto LDs. To achieve this, we used a modified RUSH system in which we anchored the membrane-embedded hairpin domain of GPAT4 at the ER (Wilfling et al., 2013). The interaction with the anchor can be released by addition of biotin to the cell-culture medium at a specific time, allowing for the analysis of a synchronous wave of proteins translocating from ER to LDs (Boncompain et al., 2012). Specifically, we used an ER membrane hook consisting of the transmembrane helix of MHC type II fused to streptavidin on its cytosolic side and attached a streptavidin-binding peptide (SBP) in tandem with a Halo-tag to the N-terminus of the *LiveDrop* hairpin *(*SBP-*LiveDrop)* (**Figure 1A)**. Co-expression of the ER hook and SBP-*LiveDrop* resulted in retention of SBP-*LiveDrop* at the ER through the streptavidin–SBP interaction, even after overnight stimulation of LD formation by incubation of cells in oleic acid–containing medium (**Figure 1B**, pre-biotin). The subsequent addition of biotin to the culture medium released SBP-*LiveDrop*, enabling visualization and measurement of synchronized ER to LD protein trafficking. Within 10 min of SBP-*LiveDrop* release, the protein re-localized from the ER to LDs, where it continued to accumulate (**Figures 1B, 1C)**, indicating membrane continuity between LDs and the ER. By 30 min, ~6–8% of the total SBP-*LiveDrop* population had relocalized to LDs. With longer biotin treatment, LD levels of SBP-*LiveDrop* continued to increase up to 25% of the total SBP-*LiveDrop*, indicating ongoing protein accumulation on the LD surface from the vast ER pool (**Figure S1A**). Comparable targeting kinetics were found for the analogous *LiveDrop* hairpin derived from human GPAT4 (**Figure S1B**).

Whether some LDs detach from the ER membrane after their formation and enter the cytoplasm has not been conclusively resolved for mammalian cells. Detached LDs should not be accessible by SBP-*LiveDrop* after biotin release*,* since this cargo is membrane-embedded and requires an ER-LD membrane contiguity to move from the ER to LDs. To analyze which fraction of LDs remains physically connected to ER at different time points of LD formation, we incubated cells with oleic acid–containing medium for a variety of times (one to 24 h) to induce LD formation and maturation. We then released SBP-*LiveDrop* from the ER and measured LD targeting after 30 min of biotin release. By measuring the amount of *SBP-LiveDrop* per LD pixel, we found that the signals were comparable, regardless of the number and size of LDs or of the time after incubation with oleate-containing medium (**Figures 1D, 1E, S1C**). Thus, each LD seemed to receive a similar amount of SBP-*LiveDrop* from the ER and that all LDs appeared physically connected to the ER during our time course.

Single-molecule tracking of SBP-*LiveDrop* with MINFLUX microscopy reveals molecular confinement on LDs despite unaffected diffusivity

Detecting the transition of SBP-*LiveDrop* from the ER to LDs using ensemble measurements is challenging, and complicates the analysis of its targeting pathway and kinetics. To overcome this limitation, we analyzed targeting of single *LiveDrop* molecules after their release from the ER. We sparsely labeled the Halo tagged SBP-*LiveDrop*-RUSH reporter with fluorescent Halo ligand JFX650 (Grimm et al., 2021). To measure molecular motion, we tracked SBP-*LiveDrop* single molecules using minimal fluorescence photon fluxes (MINFLUX) (Balzarotti et al., 2017; Schmidt et al., 2021). This system offers exceedingly high spatial and temporal resolution, enabling precise measurements of molecular motion in the ER and on LDs. We recorded 550 tracks from six

different cells (**Figure 2A, S2A),** resulting in over 2.5 million single-molecule localizations with a median time interval of 86 microseconds between consecutive measurements (**Figure S2B**), and allowing up to 12,000 single-molecule localizations under a second to assess the dynamics of protein movement (**Figure 2B**).

To analyze motion at the ER and LDs, we classified single molecule tracks based on subcellular location by masking BODIPY-positive LDs in the confocal channel (**Figure S2C**). Then, we derived mean square displacement (MSD) for individual ER and LD tracks by determining the squared distances between two localizations at increasing time intervals. To compare the 2D diffusion coefficient of *SBP-LiveDrop* in the ER and on LDs, we utilize the apparent diffusion coefficient (D_{app}) computed using the single-interval MSD as estimator (MSD = $4D_{app}$ t). SBP-*LiveDrop's* speed of the motion, reflected in the value of the apparent diffusion constant D_{app}, was unaffected by the transition of the molecule from a bilayer membrane to the monolayer, with the calculated D_{app} for LD-localized tracks similar to those at the ER ($LD_{(mean)}$ 2.78 $\mu m^2/s$, $ER_{(mean)}$ 2.82 $\mu m^2/s$) (**Figure 2C**). These values were higher than reported ER-localized proteins (Holcman et al., 2018; Obara et al., 2024; Stadler et al., 2018), possibly because the higher spatiotemporal resolution of MINFLUX tracking allowed the capture of detailed motion of the molecule with high accuracy.

In biological systems, however, the motion of molecules over time often deviates from a linear relationship between MSD and time, introducing an exponent to the time, α, converting the linear MSD-time relationship to the anomalous diffusion power law, MSD = 4 D_{app} t^{α}. If α <1, the molecule moves sub-diffusively, for instance due to geometric constraints or molecular interactions with the matrix.

We calculated the α as a proxy for the type of motion by fitting the power law equation to the entire MSD curves for each ER- and LD-localized single molecule tracks. Unexpectedly, despite similar D_{app}, we observed differences in the temporal correlations of molecular motion between the two compartments. Specifically on LDs, *SBP-LiveDrop* exhibited significant sub-diffusive behavior, where the MSD was not linearly proportional to the time passed, and instead, there was a power law effect (**Figure S2D**). Correspondingly, the mean and median α for *SBP-LiveDrop* were significantly lower on LDs (mean, α_{LD} = 0.68) than at the ER (mean, α_{ER} =0.93) (**Figure 2D, 2E**). These results show that at the molecular-lengths scale of MINFLUX measurements, SBP-*LiveDrop* becomes more confined in its motion on LDs than in the ER despite remaining similarly mobile.

SBP-*LiveDrop* molecules display distinct motion states, based on subcellular location

A limitation of MINFLUX tracking is that it tracks each molecule individually, thus limiting the number of tracks that are recorded. To enable the parallel measurement of many molecules, we extended our analysis to dual color, highly inclined and laminated optical (HILO) sheet microscopy, allowing simultaneous tracking of many single molecules in two channels. With this approach, we recorded over 56,000 SBP-*LiveDrop* trajectories containing 1.9 million single-molecule localizations from eight different cells that contained BODIPY-stained LDs at various times after biotin-mediated release from the ER hooks. To ensure accurate representation of molecular motion, we filtered out tracks less than 10 frames long (corresponding to 300 msec).

For the analysis of this large dataset, we first determined which tracks were in the ER, at LDs, or moved between both compartments. Similar to MINFLUX data analyses, we first segmented images for BODIPY-positive LDs and then categorized SBP-*LiveDrop* tracks into tracks that are only within the LD mask, outside the LD mask (ER localized), and tracks present in both locations (**Figures 3A, S3A**). The majority of SBP-*LiveDrop* single-molecule tracks localized to the ER (47,846 tracks, 85.5%), whereas 7% of the total tracks recorded (3,909 tracks) were found only on the LD (**Figure 3B**). Additionally, we observed tracks with more complex localization patterns (4,266 tracks – 7.5%), representing molecules travelling between the ER and

LDs (**Figures S3A, S3B**). Consistent with confocal imaging, we found that the fraction of tracks on LDs increased with longer biotin incubations, indicating protein accumulation on LDs over time after the release (**Figures S3C, S3D**).

The longer time scale of HILO compared to MINFLUX measurements, make it ideal to detect anomalous diffusion which is most apparent at longer observation intervals. Using single-interval MSDs calculated from HILO measurements, we calculated mean D_{app} for SBP-*LiveDrop* tracks and found them to be generally ~10-fold lower than the values with MINFLUX tracking (**Figure 3C**). This difference with smaller D_{app} values calculated from the HILO than MINFLUX data may be explained by the ~360 times slower location sampling with HILO microscopy, which masks unhindered displacements and accumulates confinement effects from spatial constraints and molecular interactions. Nevertheless, HILO measurements revealed the mean D_{app} for LD-localized SBP-*LiveDrop* tracks was lower than for ER-localized tracks (0.25 $\mu m^2/s$ versus 0.30 $\mu m^2/s$, respectively) (**Figure 3C**). Since the MSD was not linearly proportional to the time passed, particularly for longer time intervals, diffusion of SBP-*LiveDrop* as assessed by HILO microscopy was anomalous. In agreement with this possibility, analysis of MSD curves fit to power law equation with an exponent α that was lower on LDs than in the ER, indicating more sub-diffusive behavior and confinement on the monolayer surface (**Figure 3D, S4A**).

To unbiasedly analyze our SBP-*LiveDrop* tracks, we employed DeepSPT, a machine-learning-based diffusion analysis pipeline (**see Methods**) (Kæstel-Hansen et al., 2023). This analysis allowed us to segment and classify each track by the type of motion: free motion only (displays higher α), confined motion only (displays lower α), and ones that switch between the two motion states (single and multiple switches - changing α) (**Figure 3E, S4B**). Within this large dataset, different motion states correlated well with subcellular localization. As expected, confined *SBP-LiveDrop* molecules display smaller α values with lower D_{app} (**Figures 3F, 3G**). At the ER, motion signatures were mixed. Free motion was, by far, the most abundant motion state, whereas confined movement was observed more often on LDs (**Figures 3H, 3I, S4B**), indicating that the motion state of the molecule largely depends on the subcellular location.

Confinement on LDs is driven by tryptophan residues within the SBP-*LiveDrop* hairpin

The presence of several tryptophan residues in *LiveDrop* in the middle of the hydrophobic domain (**Figure S5A**), uncharacteristic for membrane segments (Arkin & Brunger, 1998; Landolt-Marticorena et al., 1993), is critical for its LD localization and accumulation (Olarte et al., 2020). We, therefore, hypothesized that these tryptophans contributed to the confined movement on LDs. To test this hypothesis, we mutated these three tryptophan residues to valines (**Figure S5A**) and imaged single molecules of this mutant (W-mut) after biotin release with HILO microscopy.

The SBP-*LiveDrop* W-mut displayed complex motion patterns similar to wild-type (WT) SBP-*LiveDrop*, with most molecules moving freely throughout the ER network (**Figures S5B, S5C**). However, the lack of tryptophan residues reduced the protein's D_{app}, compared with WT *SBP-LiveDrop*, in both compartments (**Figures 4A, S5D**). This was most prominent in the ER membrane (mean D_{app} of 0.19 $\mu m^2/s$ and 0.30 $\mu m^2/s$ for W-mut and WT, respectively), but was also found at LDs (mean D_{app} of 0.16 $\mu m^2/s$ and 0.25 $\mu m^2/s$ for W-mut and WT, respectively) (**Figures 4A, S5D**). Possibly, *SBP-LiveDrop* is not well adapted to the structure of the ER membrane and has weaker interactions with ER lipids there and hence moves faster than W-mut.

Despite overall slower motion, we observed that the SBP-*LiveDrop* W-mut traveled to the LD surface more frequently (24% of tracks for W-mut vs. 14% of tracks for WT SBP-*LiveDrop*) (**Figure S3B, S5B**). Although the α decreased when W-mut travelled from the ER to LDs (ER_{mean}: 0.99, LD_{mean}: 0.89) (**Figure 4B**), indicating its movement was also somewhat restricted in the LD environment, they remained significantly higher than the WT SBP-*LiveDrop* (WT_{mean}: 0.82, p value<0.0001) (**Figure S5E**), suggesting that tryptophan residues constrain the WT protein in this environment. Consistent with higher α on LDs, this mutant more often displayed free motion

behavior after it localized to LDs (**Figures 4C, 4D**). Additionally, the W-mut explored a smaller portion of LDs due to its tendency to freely travel between compartments and spent shorter time on LDs than the WT SBP-*LiveDrop* (**Figure 4E, S5F)**.

To test whether a change in total hydrophobicity within the hairpin would alter its confinement behavior at LDs, we analyzed single-molecule trajectories of a scrambled version of SBP-*LiveDrop,* which has the same amino acid composition as the WT hairpin, but with a scrambled sequence (Olarte et al., 2020). The scrambled hairpin had similar ER mobility to the WT SBP-*LiveDrop*, with a mean apparent 2D diffusion coefficient of 0.28 $\mu m^2/s$ (**Figures S5G**). This mutant, however, failed to access the LD surface and always stayed in the ER (**Figure S5H**), suggesting that the positioning of tryptophan residues plays a role in targeting the protein to LDs.

SBP-*LiveDrop* enters the LD surface at a single ER-LD contact site

Our single-molecule tracking studies enabled us to determine how SBP-*LiveDrop* accesses LDs. Following many individual SBP-*LiveDrop* tracks that transition from ER to LDs, we filtered data from HILO studies for tracks that were present both outside and inside BODIPY masks and then identified tracks that were classified by DeepSPT to switch from free to confined motion mid-track (**Figure 5A**). More than 200 tracks satisfied these criteria to be considered as ER-to-LD travelling tracks within our dataset. In agreement with a transition of these molecules from ER to LDs, the BODIPY signal measured along these tracks increased with motion switching (**Figure 5B**). Moreover, the apparent 2D diffusion coefficient for SBP-*LiveDrop* molecules decreased by ~30% (0.31 $\mu m^2/s$ for ER vs 0.23 $\mu m^2/s$ on LDs) upon transitioning to LD surface (**Figure 5C**), indicating a change of motion behavior.

In rare instances, we captured multiple different tracks appearing to access LDs from different directions within a short time (**Figure 5D)**. We hypothesized that multiple ER-LD membrane bridges exist at a single LD, allowing proteins to enter LDs at multiple sites. To test this hypothesis, we analyzed the coordinates of each switch from ER to LD motion pattern, indicating LD access. Contrary to our hypothesis, in the examples analyzed, the motion switch points entered BODIPY-stained LD at similar locations (**Figure 5E**), suggesting that each of these molecules accessed the LD through the same entry site.

SBP-*LiveDrop* accesses LDs via seipin-mediated membrane bridges

Seipin oligomers form a single stable focus at ER-LD interfaces (Chung et al., 2019; Klug et al., 2021; Salo et al., 2016; Wang et al., 2016) and confocal imaging in SUM159 cells confirmed that endogenously tagged seipin formed one distinct punctum adjacent to each LD (**Figure 6A**).

To test whether the entry point for SBP-*LiveDrop* to LDs was at seipin oligomers, we used HILO microscopy to simultaneously image SBP-*LiveDrop* single molecules and endogenously tagged seipin after biotin release. We observed two seipin populations with distinct motion. LD-associated seipin was far less mobile than free seipin (**Figures 6B, S6A**), potentially due to maintaining the ER-LD membrane bridge.

Because seipin is relatively static at LDs, its single molecule positions were densely clustered at areas that appear to be ER-LDs contact sites (**Figures 6C, S6B).** This allowed us to map the seipin-dense regions as a proxy for ER-LD membrane bridges and analyzed SBP-*LiveDrop* movement across these regions (**Figures 6D, 6E, S7A**). DeepSPT analysis simultaneously revealed LD localization and SBP-*LiveDrop* with changing motion signatures solely using SBP-*LiveDrop* motion characteristics (**Figure S7B)**. This analysis identified several ER-to-LD travelling SBP-*LiveDrop* tracks that also colocalized with seipin-dense regions (**Figure 6E**). As these tracks transitioned from the ER to LDs, their motion breakpoints colocalized at the focus formed by a stable, LD-associated seipin cluster (**Figure 6F)**, indicating protein movement across a seipin complex.

Seipin is required for maintaining stable bridges between the ER and LDs

Our results indicated that seipin mediates SBP-*LiveDrop* trafficking to the LD surface by forming a direct path between the ER bilayer and the LD monolayer. The absence of seipin leads to defects in LD formation and morphology (Salo et al., 2016; Szymanski et al., 2007; Wang et al., 2016) and to detachments of LDs from the ER membrane (Salo et al., 2016; Wang et al., 2016). We hypothesized that, in seipin-knockout cells, some LDs cannot receive proteins from the ER membrane due to loss of ER-LD continuity.

To test this hypothesis, we examined the behavior of SBP-*LiveDrop*-RUSH in seipin-knockout cells. Upon release from the ER, SBP-*LiveDrop* targeted to some LDs, with kinetics similar to WT LDs, whereas other LDs did not receive SBP-*LiveDrop* even 30 min after biotin-mediated release, indicating a loss of bilayer-monolayer membrane bridges (**Figure 6G**). We also observed <1% of the total SBP-*LiveDrop* on LDs after 30 min of biotin release (**Figure 6H),** compared with 6–8% in WT cells at this time (Figure 1C), which indicates that *SBP-LiveDrop* targets to fewer LDs due to loss of ER-LD contacts.

SBP-*LiveDrop* movement across seipin complexes is bidirectional

Given seipin's role in maintaining a membrane bridge that allows proteins to travel to LDs, we next asked if these bridges allow *SBP-LiveDrop* to move back to the ER. To test this hypothesis, we performed a "reverse-RUSH" experiment (**Figure 7A**). We incubated the SBP-*LiveDrop*-RUSH-expressing cells with biotin and oleic acid overnight to stimulate LD production and allow SBP-*LiveDrop* to accumulate at LDs. The following day, we pulse-labelled the LD-localized SBP-*LiveDrop* population with fluorescent Halo ligand and added excess avidin into the oleate-containing media to sequester biotin while maintaining the LD population. This allowed the ER hooks to re-capture pre-labelled SBP-*LiveDrop* molecules that escaped from LDs back to the ER. After overnight avidin incubation, almost all SBP-*LiveDrop* was retained at the ER (**Figure 7B, 7C**), indicating that SBP-*LiveDrop* molecules travelled back to the ER membrane. Cellular levels of SBP-*LiveDrop* did not change after avidin incubation, suggesting that the change in localization was not due to protein turnover (**Figure 7D**).

In agreement with these results, our single-molecule tracking dataset contained instances of SBP-*LiveDrop* molecules that travelled from an LD to the ER and also transitioned from confined to free movement (**Figures S3B, S5C**) The trajectories of these molecules exhibited decreased BODIPY signal once the confined-to-free motion switch occurred, indicating that they exit the LD at this point (**Figure 7E).** Such LD-to-ER tracks were present at every time point we measured, including ones with a short biotin incubation and later stages of biotin release (**Figure S8A).** The diffusion breakpoints of the reverse tracks were found at sites of LD entry (**Figure 7F, 7G**) and colocalized with seipin-dense regions (**Figures 7H, S8B**). These findings support a model where seipin maintains a monolayer-bilayer membrane bridge at ER-LD contact sites that allows bidirectional movement of SBP-*LiveDrop* protein cargo (**Figure 7H, 7I**).

DISCUSSION

Here we directly measured the molecular motion of an ER to LD cargo, *LiveDrop*, in its native environment, combining synchronized protein trafficking with single-molecule tracking. These approaches yielded high-resolution data that allow important conclusions concerning protein trafficking between these organelles.

The unprecedented speed of data acquisition with high spatial precision enabled by MINFLUX allowed us to analyze diffusion of SBP-*LiveDrop* in different membrane environments. Given that these the ER and LD environments have different surface properties, such as phospholipid packing and densities of proteins (Kory et al., 2016; Prévost et al., 2018), we expected that SBP-*LiveDrop* would exhibit different apparent diffusion coefficients in the two compartments. However, our studies with MINFLUX tracking revealed that SBP-*LiveDrop* appeared to move with similar speeds in both environments, reflected in the comparable apparent

diffusion coefficients D_{app}. But, over longer time sampling of individual tracks, we found that the diffusion of SBP-*LiveDrop* in the LD compartment was more anomalous, as shown by its more sub-diffusive behavior (lower α value) on LDs than with the ER. Thus, our results in this instance uncouple molecular confinement, as measured over longer time periods, from the diffusive speed of the molecule.

What could be causing molecular confinement of SBP-*LiveDrop* at LDs? A possible explanation is that there are binding and un-binding events with other molecules that impede free movement on the monolayer surface. This idea is supported by our analysis of a tryptophan mutant of SBP-*LiveDrop (*W-mut) that moves between ER and LDs but shows less confinement (increased α) on LDs than WT *SBP-LiveDrop.* We expect that expression of W-mut would not change molecular crowding of the LD surface, compared to expression of WT *SBP-LiveDrop.* Therefore, mutating the tryptophan residues likely impairs protein-lipid interactions, rather than changing molecular crowding, and leads to less sub-diffusive behavior on LDs. Consistently, our previous MD simulations of *LiveDrop* in the environment of a LD surface suggested that the central W residues (e.g., W172 in the full-length *Drosophila* GPAT4) interact with hydroxyl groups of water or ester groups of TG and occupy lower free energy states in the LD environment (Olarte et al., 2020). Our results support a model is that the tryptophans critical for LD targeting of *LiveDrop* interact with TG molecules within the LDs, and this interaction promotes confinement of the protein at LDs and contributes to its accumulation at LD surfaces (**Figure 7I**). Tryptophan residues are most often observed at the interphase of the membrane with the aqueous environment (Khemaissa et al., 2021; Sun et al., 2008; Yau et al., 1998). Thus, a change in the hairpin conformation (Dhiman et al., 2024; Olarte et al., 2020) likely allows tryptophan residues to reposition at the interface of the loosely packed LD surface, contributing to the difference in free energy between ER and LD populations.

Our confocal and single-molecule tracking data also showed that all LDs in mammalian cells normally maintain membrane connections that allow bidirectional cargo movement between the ER and LD surface. Specifically, the protein could access essentially all LDs, regardless of when they were formed. Moreover, this protein cargo apparently accessed LDs via seipin complexes, indicating seipin's multi-functional role in facilitating initial LD formation and maintaining monolayer-bilayer membrane connections (Salo et al., 2016, 2019). The latter function is supported by our previous findings (Wang et al., 2016) and observations from this study that many LDs lose their connection with the ER and detach into the cytoplasm when seipin is deleted (**Figure 6G**). Despite this, SBP-*LiveDrop* in the ER could still access some LDs in cells lacking seipin. We speculate that the protein cargo may target large LDs via "hitch-hiking" on smaller LDs that are severed from the ER and coalesce with larger LDs in the absence of seipin (Wang et al., 2016). This possibility is supported by our observation of many smaller LDs in proximity to larger LDs in seipin-knockout cells (**Figure S9).**

A limitation of this study is that it is unclear whether all ER to LD targeted proteins in mammalian cells access LDs via seipin-mediated membrane contiguities. For SBP-*LiveDrop*, the small size of its membrane-embedded domain may allow it to move between the seipin transmembrane helices without steric hindrance. Whether other ER proteins, such as full-length GPAT4, target similarly in mammalian cells is unknown. Yet at least some of the cargo proteins of the ER-to-LD pathway (e.g., Alg14, LPCAT, UBXD8) share sequence features with *LiveDrop,* suggesting they traffic the same way (Olarte et al., 2020). Our efforts to retain full-length GPAT4 in the ER with the RUSH system have so-far been unsuccessful, as the protein may have multiple LD targeting motifs and the RUSH-retained protein appears to span across ER-LD junctions (not shown).

In summary, our study employing coordinated single-molecule tracking of an ER-to-LD cargo protein provides comprehensive new insights into the mechanisms of this intercompartmental protein trafficking. Such an approach, with high degrees of spatial and

temporal resolution, should be applicable to other membrane proteins that traffic between organelles.

ACKNOWLEDGEMENTS

We thank members of Harper and Farese & Walther laboratories for helpful discussions, specifically Dr. Henning Arlt and Dr. Jeeyun Chung for discussions on seipin and relevant reagents, Dr. Pedro Manuel Carpio Malia for *LiveDrop* and GPAT4 discussions, and Dr. Kelsey Hickey for scientific input and helpful discussions. We thank Dr. Talley Lambert at the Center of Imaging Technologies and Education (CITE) at Harvard Medical School for confocal and single-molecule imaging help, and Dr. Luke Lavis for Janelia Fluor dyes. This work was supported by NIH R01 grants GM124348 (R.V.F), GM097194 (T.C.W), and NS083524 (J.W.H.), NNF challenge grant NNF23OC0081287 (NSH), NNF infrastructure grant NNF22OC0075851 (NSH), Vellux foundation 18333 (NSH) and by generous support from Ned Goodnow (J.W.H.). A.M. is a Helen Hay Whitney Foundation fellow and T.C.W. is a Howard Hughes Medical Institute investigator.

AUTHOR CONTRIBUTIONS

A.M., T.C.W., and R.V.F. conceived, designed, and interpreted the experiments and wrote the manuscript, with input from all authors. A.M. conceptualized, designed and conducted experiments, many of which were performed during an extended stay in the laboratory of J.W.H. J.M. performed MINFLUX data acquisition. A.M. performed MINFLUX analysis. J.K.H. performed DeepSPT analysis, instance segmentation, and track classification. A.M. and J.K.H. performed image analysis, statistics, and data visualization. J.W.H. and N.S.H. provided intellectual feedback and engaged in discussions throughout.

DECLARATION OF INTERESTS

J.M. is an employee of the company Abberior Instruments America, which commercializes super-resolution microscopy systems, including MINFLUX.

REFERENCES

Arkin, I. T., & Brunger, A. T. (1998). Statistical analysis of predicted transmembrane α-helices. *Biochimica et Biophysica Acta - Protein Structure and Molecular Enzymology*, *1429*(1). https://doi.org/10.1016/S0167-4838(98)00225-8

Balzarotti, F., Eilers, Y., Gwosch, K. C., Gynnå, A. H., Westphal, V., Stefani, F. D., Elf, J., & Hell, S. W. (2017). Nanometer resolution imaging and tracking of fluorescent molecules with minimal photon fluxes. *Science*, *355*(6325). https://doi.org/10.1126/science.aak9913

BasuRay, S., Wang, Y., Smagris, E., Cohen, J. C., & Hobbs, H. H. (2019). Accumulation of PNPLA3 on lipid droplets is the basis of associated hepatic steatosis. *Proceedings of the National Academy of Sciences of the United States of America*, *116*(19). https://doi.org/10.1073/pnas.1901974116

Boncompain, G., Divoux, S., Gareil, N., De Forges, H., Lescure, A., Latreche, L., Mercanti, V., Jollivet, F., Raposo, G., & Perez, F. (2012). Synchronization of secretory protein traffic in populations of cells. *Nature Methods*, *9*(5). https://doi.org/10.1038/nmeth.1928

Carpenter, A. E., Jones, T. R., Lamprecht, M. R., Clarke, C., Kang, I. H., Friman, O., Guertin, D. A., Chang, J. H., Lindquist, R. A., Moffat, J., Golland, P., & Sabatini, D. M. (2006). CellProfiler: Image analysis software for identifying and quantifying cell phenotypes. *Genome Biology*, *7*(10). https://doi.org/10.1186/gb-2006-7-10-r100

Chorlay, A., & Thiam, A. R. (2020). Neutral lipids regulate amphipathic helix affinity for model lipid droplets. *Journal of Cell Biology*, *219*(4). https://doi.org/10.1083/JCB.201907099

Chung, J., Wu, X., Lambert, T. J., Lai, Z. W., Walther, T. C., & Farese, R. V. (2019). LDAF1 and Seipin Form a Lipid Droplet Assembly Complex. *Developmental Cell*, *51*(5). https://doi.org/10.1016/j.devcel.2019.10.006

Čopič, A., Antoine-Bally, S., Giménez-Andrés, M., La Torre Garay, C., Antonny, B., Manni, M. M., Pagnotta, S., Guihot, J., & Jackson, C. L. (2018). A giant amphipathic helix from a perilipin that is adapted for coating lipid droplets. *Nature Communications*, *9*(1). https://doi.org/10.1038/s41467-018-03717-8

Dhiman, R., Perera, R. S., Poojari, C. S., Wiedemann, H. T. A., Kappl, R., Kay, C. W. M., Hub, J. S., & Schrul, B. (2024). Hairpin protein partitioning from the ER to lipid droplets involves major structural rearrangements. *Nature Communications*, *15*(1), 4504. https://doi.org/10.1038/s41467-024-48843-8

Ershov, D., Phan, M. S., Pylvänäinen, J. W., Rigaud, S. U., Le Blanc, L., Charles-Orszag, A., Conway, J. R. W., Laine, R. F., Roy, N. H., Bonazzi, D., Duménil, G., Jacquemet, G., & Tinevez, J. Y. (2022). TrackMate 7: integrating state-of-the-art segmentation algorithms into tracking pipelines. *Nature Methods*, *19*(7). https://doi.org/10.1038/s41592-022-01507-1

Grimm, J. B., Xie, L., Casler, J. C., Patel, R., Tkachuk, A. N., Falco, N., Choi, H., Lippincott-Schwartz, J., Brown, T. A., Glick, B. S., Liu, Z., & Lavis, L. D. (2021). A General Method to Improve Fluorophores Using Deuterated Auxochromes. *JACS Au*, *1*(5). https://doi.org/10.1021/jacsau.1c00006

Holcman, D., Parutto, P., Chambers, J. E., Fantham, M., Young, L. J., Marciniak, S. J., Kaminski, C. F., Ron, D., & Avezov, E. (2018). Single particle trajectories reveal active endoplasmic reticulum luminal flow. In *Nature Cell Biology* (Vol. 20, Issue 10). https://doi.org/10.1038/s41556-018-0192-2

Kæstel-Hansen, J., Sautu, M. de, Saminathan, A., Scanavachi, G., Correia, R. F. B. D. C., Nielsen, A. J., Bleshøy, S. V., Boomsma, W., Kirchhausen, T., & Hatzakis, N. S. (2023). Deep learning assisted single particle tracking for automated correlation between diffusion and function. *BioRxiv*, 2023.11.16.567393. https://doi.org/10.1101/2023.11.16.567393

Khemaissa, S., Sagan, S., & Walrant, A. (2021). Tryptophan, an amino-acid endowed with unique properties and its many roles in membrane proteins. In *Crystals* (Vol. 11, Issue 9). https://doi.org/10.3390/cryst11091032

Kim, S., & Swanson, J. M. J. (2020). The Surface and Hydration Properties of Lipid Droplets. *Biophysical Journal*, *119*(10). https://doi.org/10.1016/j.bpj.2020.10.001

Klug, Y. A., Deme, J. C., Corey, R. A., Renne, M. F., Stansfeld, P. J., Lea, S. M., & Carvalho, P. (2021). Mechanism of lipid droplet formation by the yeast Sei1/Ldb16 Seipin complex. *Nature Communications*, *12*(1). https://doi.org/10.1038/s41467-021-26162-6

Kory, N., Farese, R. V., & Walther, T. C. (2016). Targeting Fat: Mechanisms of Protein Localization to Lipid Droplets. In *Trends in Cell Biology* (Vol. 26, Issue 7). https://doi.org/10.1016/j.tcb.2016.02.007

Landolt-Marticorena, C., Williams, K. A., Deber, C. M., & Reithmeier, R. A. F. (1993). Non-random distribution of amino acids in the transmembrane segments of human type I single span membrane proteins. In *Journal of Molecular Biology* (Vol. 229, Issue 3). https://doi.org/10.1006/jmbi.1993.1066

Ma, Y., Belyaeva, O. V., Brown, P. M., Fujita, K., Valles, K., Karki, S., de Boer, Y. S., Koh, C., Chen, Y., Du, X., Handelman, S. K., Chen, V., Speliotes, E. K., Nestlerode, C., Thomas, E., Kleiner, D. E., Zmuda, J. M., Sanyal, A. J., Kedishvili, N. Y., … Rotman, Y. (2019). 17-Beta Hydroxysteroid Dehydrogenase 13 Is a Hepatic Retinol Dehydrogenase Associated With Histological Features of Nonalcoholic Fatty Liver Disease. *Hepatology*, *69*(4). https://doi.org/10.1002/hep.30350

Obara, C. J., Nixon-Abell, J., Moore, A. S., Riccio, F., Hoffman, D. P., Shtengel, G., Xu, C. S., Schaefer, K., Pasolli, H. A., Masson, J. B., Hess, H. F., Calderon, C. P., Blackstone, C., &

Lippincott-Schwartz, J. (2024). Motion of VAPB molecules reveals ER–mitochondria contact site subdomains. *Nature*, *626*(7997). https://doi.org/10.1038/s41586-023-06956-y

Olarte, M. J., Kim, S., Sharp, M. E., Swanson, J. M. J., Farese, R. V., & Walther, T. C. (2020). Determinants of Endoplasmic Reticulum-to-Lipid Droplet Protein Targeting. *Developmental Cell*, *54*(4). https://doi.org/10.1016/j.devcel.2020.07.001

Olzmann, J. A., Richter, C. M., & Kopito, R. R. (2013). Spatial regulation of UBXD8 and p97/VCP controls ATGL-mediated lipid droplet turnover. *Proceedings of the National Academy of Sciences of the United States of America*, *110*(4). https://doi.org/10.1073/pnas.1213738110

Prévost, C., Sharp, M. E., Kory, N., Lin, Q., Voth, G. A., Farese, R. V., & Walther, T. C. (2018). Mechanism and Determinants of Amphipathic Helix-Containing Protein Targeting to Lipid Droplets. *Developmental Cell*, *44*(1). https://doi.org/10.1016/j.devcel.2017.12.011

Rowe, E. R., Mimmack, M. L., Barbosa, A. D., Haider, A., Isaac, I., Ouberai, M. M., Thiam, A. R., Patel, S., Saudek, V., Siniossoglou, S., & Savage, D. B. (2016). Conserved amphipathic helices mediate lipid droplet targeting of perilipins 1-3. *Journal of Biological Chemistry*, *291*(13). https://doi.org/10.1074/jbc.M115.691048

Ruggiano, A., Mora, G., Buxó, L., & Carvalho, P. (2016). Spatial control of lipid droplet proteins by the ERAD ubiquitin ligase Doa10 . *The EMBO Journal*, *35*(15). https://doi.org/10.15252/embj.201593106

Salo, V. T., Belevich, I., Li, S., Karhinen, L., Vihinen, H., Vigouroux, C., Magré, J., Thiele, C., Hölttä-Vuori, M., Jokitalo, E., & Ikonen, E. (2016). Seipin regulates ER –lipid droplet contacts and cargo delivery . *The EMBO Journal*, *35*(24). https://doi.org/10.15252/embj.201695170

Salo, V. T., Li, S., Vihinen, H., Hölttä-Vuori, M., Szkalisity, A., Horvath, P., Belevich, I., Peränen, J., Thiele, C., Somerharju, P., Zhao, H., Santinho, A., Thiam, A. R., Jokitalo, E., & Ikonen, E. (2019). Seipin Facilitates Triglyceride Flow to Lipid Droplet and Counteracts Droplet Ripening via Endoplasmic Reticulum Contact. *Developmental Cell*, *50*(4). https://doi.org/10.1016/j.devcel.2019.05.016

Schindelin, J., Arganda-Carreras, I., Frise, E., Kaynig, V., Longair, M., Pietzsch, T., Preibisch, S., Rueden, C., Saalfeld, S., Schmid, B., Tinevez, J. Y., White, D. J., Hartenstein, V., Eliceiri, K., Tomancak, P., & Cardona, A. (2012). Fiji: An open-source platform for biological-image analysis. In *Nature Methods* (Vol. 9, Issue 7). https://doi.org/10.1038/nmeth.2019

Schmidt, R., Weihs, T., Wurm, C. A., Jansen, I., Rehman, J., Sahl, S. J., & Hell, S. W. (2021). MINFLUX nanometer-scale 3D imaging and microsecond-range tracking on a common fluorescence microscope. *Nature Communications*, *12*(1). https://doi.org/10.1038/s41467-021-21652-z

Song, J., Mizrak, A., Lee, C. W., Cicconet, M., Lai, Z. W., Tang, W. C., Lu, C. H., Mohr, S. E., Farese, R. V., & Walther, T. C. (2022). Identification of two pathways mediating protein targeting from ER to lipid droplets. *Nature Cell Biology*, *24*(9). https://doi.org/10.1038/s41556-022-00974-0

Stadler, L., Speckner, K., & Weiss, M. (2018). Diffusion of Exit Sites on the Endoplasmic Reticulum: A Random Walk on a Shivering Backbone. *Biophysical Journal*, *115*(8). https://doi.org/10.1016/j.bpj.2018.09.007

Stirling, D. R., Swain-Bowden, M. J., Lucas, A. M., Carpenter, A. E., Cimini, B. A., & Goodman, A. (2021). CellProfiler 4: improvements in speed, utility and usability. *BMC Bioinformatics*, *22*(1). https://doi.org/10.1186/s12859-021-04344-9

Sun, H., Greathouse, D. V., Andersen, O. S., & Koeppe, R. E. (2008). The Preference of Tryptophan for Membrane Interfaces. *Journal of Biological Chemistry*, *283*(32). https://doi.org/10.1074/jbc.m802074200

Szymanski, K. M., Binns, D., Bartz, R., Grishin, N. V., Li, W. P., Agarwal, A. K., Garg, A., Anderson, R. G. W., & Goodman, J. M. (2007). The lipodystrophy protein seipin is found at

endoplasmic reticulum lipid droplet junctions and is important for droplet morphology. *Proceedings of the National Academy of Sciences of the United States of America*, *104*(52). https://doi.org/10.1073/pnas.0704154104

Tinevez, J. Y., Perry, N., Schindelin, J., Hoopes, G. M., Reynolds, G. D., Laplantine, E., Bednarek, S. Y., Shorte, S. L., & Eliceiri, K. W. (2017). TrackMate: An open and extensible platform for single-particle tracking. *Methods*, *115*. https://doi.org/10.1016/j.ymeth.2016.09.016

Van Der Walt, S., Schönberger, J. L., Nunez-Iglesias, J., Boulogne, F., Warner, J. D., Yager, N., Gouillart, E., & Yu, T. (2014). Scikit-image: Image processing in python. *PeerJ*, *2014*(1). https://doi.org/10.7717/peerj.453

Wang, H., Becuwe, M., Housden, B. E., Chitraju, C., Porras, A. J., Graham, M. M., Liu, X. N., Thiam, A. R., Savage, D. B., Agarwal, A. K., Garg, A., Olarte, M. J., Lin, Q., Frohlich, F., Hannibal-Bach, H. K., Upadhyayula, S., Perrimon, N., Kirchhausen, T., Ejsing, C. S., … Farese, R. V. (2016). Seipin is required for converting nascent to mature lipid droplets. *ELife*, *5*(AUGUST). https://doi.org/10.7554/eLife.16582

Wilfling, F., Thiam, A. R., Olarte, M. J., Wang, J., Beck, R., Gould, T. J., Allgeyer, E. S., Pincet, F., Bewersdorf, J., Farese, R. V., & Walther, T. C. (2014). Arf1/COPI machinery acts directly on lipid droplets and enables their connection to the ER for protein targeting. *ELife*, *2014*(3). https://doi.org/10.7554/eLife.01607

Wilfling, F., Wang, H., Haas, J. T., Krahmer, N., Gould, T. J., Uchida, A., Cheng, J. X., Graham, M., Christiano, R., Fröhlich, F., Liu, X., Buhman, K. K., Coleman, R. A., Bewersdorf, J., Farese, R. V., & Walther, T. C. (2013). Triacylglycerol synthesis enzymes mediate lipid droplet growth by relocalizing from the ER to lipid droplets. *Developmental Cell*, *24*(4). https://doi.org/10.1016/j.devcel.2013.01.013

Yau, W. M., Wimley, W. C., Gawrisch, K., & White, S. H. (1998). The preference of tryptophan for membrane interfaces. *Biochemistry*, *37*(42). https://doi.org/10.1021/bi980809c

Zimmermann, R., Strauss, J. G., Haemmerle, G., Schoiswohl, G., Birner-Gruenberger, R., Riederer, M., Lass, A., Neuberger, G., Eisenhaber, F., Hermetter, A., & Zechner, R. (2004). Fat mobilization in adipose tissue is promoted by adipose triglyceride lipase. *Science*, *306*(5700). https://doi.org/10.1126/science.1100747

METHOD DETAILS

Chemicals

Janelia Fluor dyes with HaloTag JFX544 and JFX650 (Grimm et al., 2021) were generous gifts from Luke Lavis (Janelia Research Campus). BODIPY 493/503 (D3922) and HCS Lipid TOX Deep Red Neutral Lipid Stain (H34477) were purchased from Thermo Fisher Scientific. AUTOdot (SM1000b) was purchased from Abgent. Avidin (A9275) and biotin (B4501), fatty acid-free BSA (A6003) and oleic acid (O1008) were purchased from Sigma-Aldrich.

An oleic acid stock solution was prepared at a stock concentration of 10 mM in 3 mM fatty acid–free BSA-PBS solution. The solution was incubated in 37°C shaking incubator for at least 1 h to dissolve fatty acids, filtered through a 0.22-µm filter, aliquoted and stored in -20°C.

For RUSH experiments, a 10 µM avidin stock solution was prepared by dissolving the lyophilized powder in sterile PBS and stored in -80°C. An 80 mM biotin solution (1000X) was prepared in DMSO and stored in -20°C.

Plasmids construction

All PCRs were performed using Q5 High Fidelity DNA Polymerase (M0491- NEB) and restriction enzymes from New England Biolabs. SBP-*LiveDrop*, scrambled and W-mut constructs for RUSH experiments were generated by amplifying ER hook from Str-ii vector (65300 - Addgene) and SBP-*LiveDrop* RUSH construct from a geneBlock (IDT). The inserts were cloned into a pLVX lentiviral expression vector (134665 Addgene) using HiFi Assembly (E5520 - NEB).

Lentiviral production

Lentivirus was produced by transfecting HEK293T with pLVX lentiviral plasmid containing RUSH constructs and standard packaging vectors using *Trans*IT-LTI Transfection Reagent (Mirus, MIR 2306). Viral particles in the supernatant was harvested at 2 days after transfection and stored frozen at -80°C until used for infection.

Cell culture

SUM159 human breast cancer cells were kindly gifted by the laboratory of Tomas Kirchhausen (Harvard Medical School) and maintained in DMEM/F-12 GlutaMAX (Life Technologies, #10565042) with 5 µg/ml insulin (Cell Applications), 1 µg/ml hydrocortisone (Sigma), 5% FBS (Life Technologies 10082147; Thermo Fisher), 50 µg/ml streptomycin, and 50 U/ml penicillin. Cells were maintained in a 5% CO_2 incubator at 37°C and at <70% confluent. To induce TG synthesis, cells were treated with growth medium containing 250 µM oleic acid complexed with fatty acid–free BSA.

Stable cell line generation

SUM159 cell lines stably expressing RUSH constructs were generated with lentiviral transduction. In brief, cells were plated into six-well plates in growth media 2 days before virus introduction. On the day of transduction, cells were treated with 8 µg/ml Polybrene (TR-1003) for 5 mins and incubated with viral supernatant for 2 days. Cells were given 4 days to express the constructs, followed by population sorting using fluorescence-activated cell sorting (FACS) on a SONY SH800S sorter. Sorted populations were confirmed with fluorescent microscopy prior to experiments.

Live cell imaging

SUM159 cells were plated on 35-mm glass-bottom dishes (MatTek Corp). Before imaging, growth medium was replaced with phenol-free DMEM/F12 medium containing 15 mM HEPES 7.5,

5 µg/ml insulin, 1 µg/ml hydrocortisone, 5% FBS, 50 µg/ml streptomycin, and 50 U/ml penicillin to prevent background fluorescence. For Halo tag labelling, cells were incubated with growth medium containing 100 nM Halo ligand as indicated, followed by three washes with label-free growth medium. For lipid droplet staining, cells were treated with BODIPY 493/503 (D3922, Thermo Fisher Scientific) or HCS LipidTOX™ Deep Red Neutral Lipid Stain (H34477, Thermo Fisher Scientific) at a 1:1000 dilution for 1 h prior to imaging. As indicated, 1 µg/mL Hoechst 33342 (H3570, Thermo Fisher Scientific) was added to growth medium for nuclear labelling.

Live cell imaging was performed using a Nikon Eclipse Ti inverted microscope equipped with Perfect Focus, a CSU-X1 spinning disk confocal head (Yokogawa), Zyla 4.2 Plus (Andor) or Orca-FUSION (Hamamatsu) sCMOS cameras, and controlled by NIS-Elements software (Nikon). The microscope is equipped with a live chamber (OkoLabs) to maintained cells at 37°C and 5% CO_2. Images were acquired through 100× Plan Apo 1.40 NA objective (Nikon). Cells were excited with solid state lasers (405-, 488-, 560-, or 640-nm - Agilent). Multicolor images were acquired sequentially.

LiveDrop RUSH assay

To retain *SBP-LiveDrop* or other constructs at the ER membrane, cells were incubated with media containing 250 µM oleic acid and 50 nM avidin (21121, Sigma) overnight to induce LD formation and sequester free biotin in the growth media, respectively. The next day, cells were labelled with the indicated Halo ligands, washed three times with fresh media containing 50 nM avidin, and incubated in media containing 250 µM oleic acid, 1 µM BODIPY 493/503 and 50 nM avidin. Release from the ER was initiated by adding 80 µM of biotin (B4501, Sigma) into the imaging dish dropwise with a tubing attached to a syringe to prevent any shift in the imaging plane. Image acquisition was started immediately upon biotin release. For kinetics experiments, images were taken every 2 min unless noted. For monitoring Seipin KO LD movement, continuous image acquisition (four frames/sec) was employed.

Pulse-chase reverse RUSH experiments were performed with cells grown in media containing 250 µM oleic acid and 1 µM of biotin overnight to allow *SBP-LiveDrop* to localize to LDs. Next day, cells were labelled with 100 nM JFX554 Halo ligand for 1 h, washed three times with fresh media, and incubated with oleic acid–containing media supplemented with PBS or avidin overnight to sequester any remaining biotin and allow ER hook to capture pre-labelled *SBP-LiveDrop* at the ER. At 1 h before imaging, 1 µM BODIPY 493/503 was added to cells to label LDs, and live cells were imaged with a confocal microscope.

MINFLUX tracking and data analysis

MINFLUX data were recorded on a commercial Abberior Instruments MINFLUX setup (Abberior Instruments GmbH), similar to the one reported by Schmidt et al. (Schmidt et al., 2021). The system was equipped with a 60x/1.4 NA magnification oil immersion lens, a 640 nm continuous-wave laser for exciting JFX650-labeled *SBP-LiveDrop* in both confocal and MINFLUX mode, and a 488 nm pulsed laser to image lipid droplets in confocal mode, with a pixel size of 50 nm. MINFLUX tracking was performed with the standard 2D 'fast' tracking sequence provided by Abberior Instruments by increasing 640 nm laser power over the subsequent iterations. The single molecule emission was detected at 653–750 nm with the pinhole set to 0.60 AU. Before and after the actual MINFLUX tracking measurements, confocal images of the lipid droplets were acquired to serve as a reference for the subcellular context. The sample position was actively stabilized on the back-scattered light of gold beads illuminated with 980 nm in widefield mode. The Abberior Instruments Inspector software with MINFLUX drivers was used to operate the system.

Single-molecule coordinates of MINFLUX tracks were analyzed using a custom python script. Confocal images for BODIPY channel were masked using OpenCV, and single molecule coordinates were categorized using the LD mask coordinates. Apparent 2D diffusion was

calculated using single-step MSD for individual ER and LD tracks. Type of motion was analyzed by fitting entire MSD curves of individual tracks to a power law equation. Fit parameters and statistical significance were calculated using the SciPy module.

Sparse labeling and single-molecule imaging

For single-molecule experiments, SUM159 cells that stably express RUSH constructs were prepared similar to above with the following modifications. To achieve single-molecule labeling, cells were incubated with 50-80 pM JFX554 or JFX650 (Grimm et al., 2021) for 30 min and washed three times with media containing 50 nM avidin. Cells were incubated with growth medium containing 250 μM oleic acid for 3 h to induce LD formation. LDs were labelled with 1 μM BODIPY 493/503 30 min prior to imaging.

Single-molecule imaging was performed using Nikon Ti motorized inverted microscope equipped with Agilent MLC 400B Laser unit (405/488/561/635), ImageEM EM-CCD camera (Hamamatsu) fitted with a 100×, NA 1.49 Apo TIRF objective lens (Nikon) combined with a 1.5x tube lens (image pixel size 0.107 μm). The angle of illumination was optimized to achieve full depth-of-focus of the objective lens with low SNR. Simultaneous dual color imaging experiments were performed with a dual view mirror setup (Optical Insights, AZ) equipped with either a 565LP dichroic mirror in series with 525/50 (left) and 600/50m (right) (for JFX554) or a 610LP dichroic mirror followed by 525/50 (left) and 645/75m (right) (for JFX650) Chroma filters for optimal channel separation. Single-molecule images were captured with high EM gain with 30ms exposure time with no delay acquisition to achieve a framerate of 31fps.

Image quantification and track generation

All acquired images were processed and prepared for figures using Fiji (Schindelin et al., 2012). Confocal images were quantified using CellProfiler (Carpenter et al., 2006; Stirling et al., 2021)software with a custom pipeline, including image enhancement, object identification for LD, mask segmentation and quantification of channel intensities to measure SBP-*LiveDrop* intensity on LDs. Colocalization was measured using Mander's coefficient calculation.

Single-molecule tracks were generated using Fiji TrackMate plugin (Ershov et al., 2022; Tinevez et al., 2017). Tracks were generated using LAP tracker with a 0.5-μm search radius for each single-molecule spot combined with gap filling of four frames within 0.7-μm radius. Initial filtering was performed using a custom Python script to filter out tracks shorter than 10 frames. Combined tracks were exported in .csv format and analyzed in DeepSPT modules (below).

Instance segmentation images to capture LDs

To accurately segment LDs with varying sizes, we utilized a deep-learning framework Stardist, which is pre-trained to be a versatile segmentation tool in fluorescent microscopy. Each identified LD per frame was converted into a binary mask of zeros for background and a single unique integer for the pixels it occupies. Only LDs of fewer than 150 pixels were considered unless LDs have grouped inseparably close or Seipin has been knocked out, promoting LDs, in which case large masks were kept. The unique masks identified per frame were tracked in time using Trackpy's nearest neighbor linking, with a search range of 5 or 10 pixels depending on visual evaluation and, thus, resulting in a time-persistent unique identifier per LD. The annotation of pixels to either ER or a time-persistent unique LD identifier enables the evaluation of the cellular localization of each SBP-*LiveDrop* track with individual LD resolution.

Deep-learning-assisted analysis of temporal diffusional behavior

The diffusion of SBP-*LiveDrop* is highly heterogeneous with large spatiotemporal variation in diffusional behavior especially dependent on the cellular localization of SBP-*LiveDrop* (i.e., ER-bound or LD bound). Therefore, to analyze the diffusional properties and temporal behavior of SBP-*LiveDrop* as it travels the ER and LDs, a deep-learning-assisted framework termed

DeepSPT (Kæstel-Hansen et al., 2023) was employed, which is designed for analysis and interpretation of heterogeneous single-particle diffusion. DeepSPT is a multi-modular deep learning framework consisting of three main modules: 1) time-resolved predictions of diffusional behavior, 2) quantification of diffusional properties, and 3) a downstream classifier utilizing the first two modules and experimental data to learn a system-specific task.

Temporal segmentation and quantification of diffusional behavior

DeepSPT is rigorously pre-trained to transform raw 2D or 3D trajectories into a diffusional behavior prediction and probability estimate per time point. To analyze temporal diffusion behavior, SBP-*LiveDrop* single-particle trajectories were fed directly to the fully convolutional end-to-end temporal segmentation module of DeepSPT. The diffusion of SBP-*LiveDrop* on ER or LDs is quite complex consisting of different modes of diffusion yet is more restricted on LDs due to their size. Therefore, given the task of delineating ER and LD diffusion any Brownian or directed motion is considered "Free" behavior and any subdiffusive or confined diffusion is considered "Restricted". These time-resolved predictions of free and restricted behavior enable diffusional change point analysis and the correlation of diffusional behavior to cellular localization. Diffusional fingerprints for each trajectory was analyzed using the second module of DeepSPT. This diffusional quantification includes features, such as: the diffusion coefficient was driven from single interval MSD, anomalous diffusion exponent via power law equation $MSD = 4Dt^{a}$, explored area of trajectories, and number of times a behavior is sampled.

DeepSPT feature representation of SBP-*LiveDrop* trajectories

Combining the first two modules of DeepSPT allows the embedding of trajectories into fixed length feature representations, of both temporal and diffusional features, suitable for machine learning classification. Specifically, the resulting representation of each trajectory combines: Statistics on the behavior transition sequence and the number of times a trajectory samples either a free or restricted diffusional state. In addition, the diffusional features over the entire trajectory length and the average of features for free and restricted segments are concatenated to the representation.

Classification of trajectory cellular location solely by diffusion and model validation

DeepSPT's third module utilizes the feature representation derived from the first two modules to provide classification directly using experimental data. The downstream classifier employed for the prediction of SBP-*LiveDrop's* cellular localization consists of an ensemble of three Random Forest classifiers each consisting of 100 tree estimators and with maximum tree depth of 5, 6, and 7, respectively. The final ensemble prediction is taken as the mode prediction of the three classifiers. To overcome biased predictions due to class imbalance as the majority of SBP-*LiveDrop* tracks are on the ER, random oversampling of the minority class is implemented. Model performance is evaluated using leave-one-group-out cross-validation where each group is a biological replicate (i.e., an independent TIRF single-particle-tracking experiment) to confirm the model's ability to generalize across experimental variability and to unseen cells.

Identification of LD-associated seipin

LD-associated seipin complexes were identified using positional density and diffusional traits. First, seipin trajectories classified by DeepSPT to exhibit free diffusion for more than 90% of their track duration were filtered out. Then, a two-dimensional (2D) histogram representing the spatiotemporal localizations of seipin was constructed, resulting in a heatmap of positional density of seipin. Next, this heatmap was binarized using an experiment-dependent threshold to simplify detection of seipin dense areas by Laplacian of the Gaussian using scikit-image (Van Der Walt et al., 2014) with maximum sigma of 2 and threshold of 0.1.

Evaluation of linking error potential

Evaluation of linking error potential was performed by calculating the distance from every individual SBP-*LiveDrop* detection in frame, *i*, to every detection in frame, *i+1*, and counting the number of detections within the SBP-*LiveDrop* tracking search range.

Statistics

Unless otherwise stated, results are presented as mean ± standard deviation. Statistical analyses of results were performed using SciPy statistics package in Python. Statistical tests used for analysis are indicated in Figure legends. Statistically significant calculations were denoted with * for $p<0.05$, ** for $p<0.01$, *** for $p<0.001$, **** for $p<0.0001$. Actual p values are included in the figures.

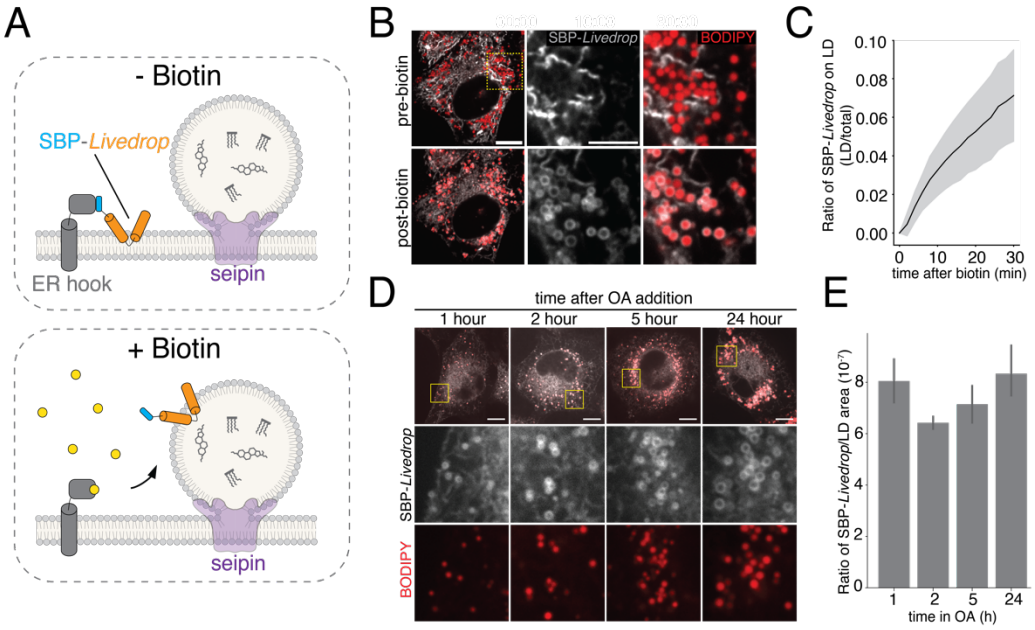

Figure 1. Synchronized LD cargo release reveals that all LDs are connected to the ER and receive protein cargo.

A) Illustration of synchronized trafficking of *SBP-LiveDrop* from the ER to LDs using RUSH. SBP-*LiveDrop* retention on the ER membrane is achieved via the interaction with the ER hook. Biotin addition into the growth medium releases SBP-*LiveDrop* by competing for streptavidin binding and, thus, allows real-time monitoring of SBP-*LiveDrop* trafficking to LD surface.

B) Live-cell confocal microscopy images of SBP-*LiveDrop* before and 10 min after biotin release. Cells were treated with 250 μM oleic acid to induce LD formation overnight. *SBP-LiveDrop* was labeled with JFX554 Halo ligand and released by adding 80 μM biotin into the imaging medium. LDs were labelled with 1 μM BODIPY 493/503. Scale bars: left: 10 μm, right: 5 μm.

C) Quantification of the targeting kinetics of *SBP-LiveDrop* after biotin release. Targeting ratio was calculated by dividing *SBP-LiveDrop* levels within the BODIPY mask to total intensity, then normalized to pre-release levels. n = 35.

D) SBP-*LiveDrop* targets to every nascent and mature LD after biotin release. Cells were incubated with 250 μM oleic acid for indicated amounts of time to initiate LD formation, followed by biotin release for 30 mins prior to imaging with a confocal microscope. LDs were labelled with 1 μM BODIPY 493/503. Scale bar: 10 μm.

E) Quantification of *SBP-LiveDrop* levels on LDs after 30-min biotin release. Targeting ratio was divided to total BODIPY mask area for each image to calculate the amount of *SBP-LiveDrop* per LD area.

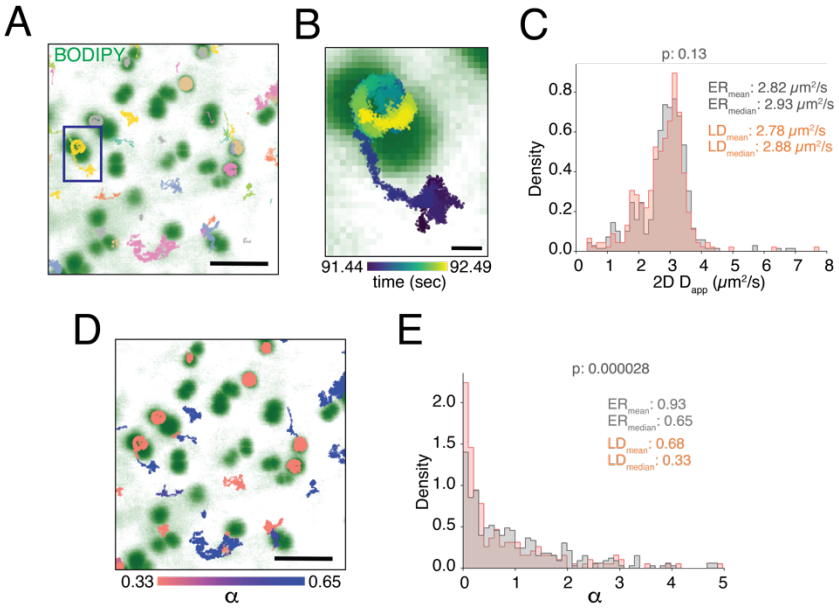

Figure 2. Single-molecule tracking of *SBP-LiveDrop* with MINFLUX reveals similar mobility at the ER and LDs

A) Representative MINFLUX single-molecule tracks are plotted on LD channel (green). Tracks are colored individually. Prior to imaging, cells were treated with 250 µM oleic acid to induce LD formation and labeled with 50 pM JFX650. LDs were stained with 1 µM BODIPY 493/503. Scale bar: 2 µm.

B) Zoomed in *SBP-LiveDrop* track from Figure 2A. Each single-molecule localization is colored based on the time stamp. Scale bar: 250 nm.

C) Distribution of the apparent 2D diffusion coefficients for the ER (grey) and LD (orange) localized *SBP-LiveDrop* tracks recorded with MINFLUX imaging. A two-sided Mann-Whitney U-test was performed to compare ER and LD values. p = 0.13.

D) Single-molecule tracks from 2A are colored, based on their α values. Color bar limits represent median values for LD (left) and ER (right) tracks.

E) Distribution of the α exponent of the power law equation derived from the MSD curves for individual ER (grey) and LD (orange) localized tracks. A two-sided Mann-Whitney U-test was performed to compare ER and LD values. p = 0.000028.

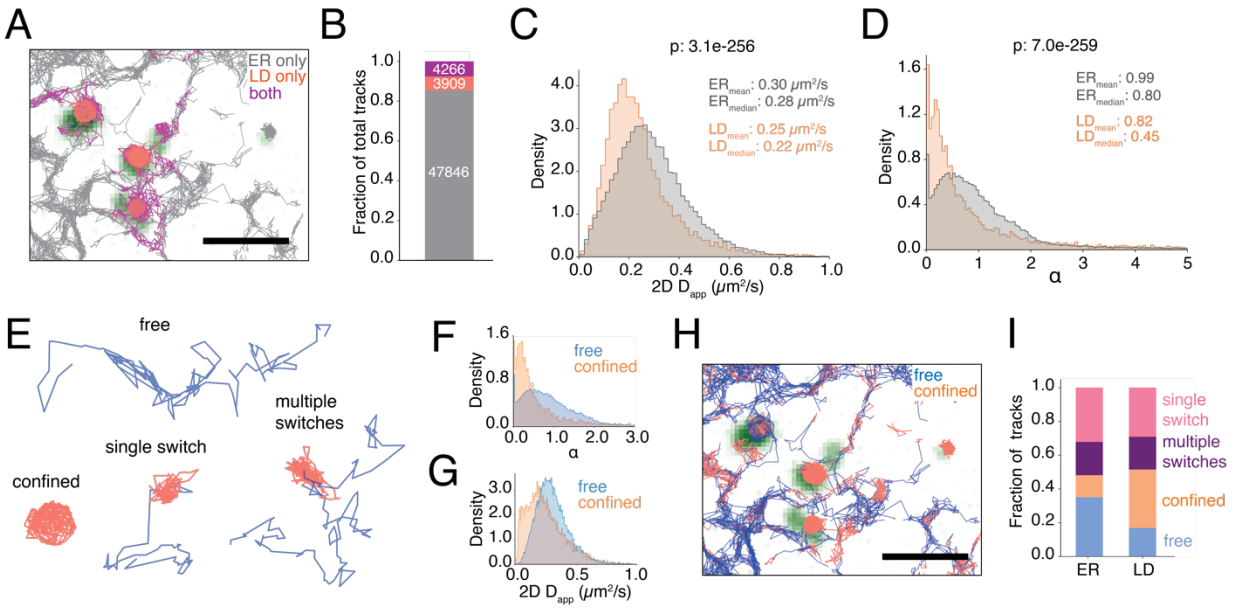

Figure 3. *SBP-LiveDrop* displays distinct motion states based on subcellular location

A) Single-tracks of SBP-*LiveDrop* recorded 25 min post-biotin using a HILO microscope. Cells were induced with 250 μM oleic acid for 3 h to form LDs and labelled with BODIPY 493/503 (green), and single SBP-*LiveDrop* molecules were imaged with a HILO microscope. Tracks are colored, based on their subcellular location. Orange: LD tracks, grey: ER tracks, magenta: tracks that are present in both locations. The number of tracks recorded for each category is displayed on a stacked bar graph (right). Scale = 2 μm.

B) Single-molecule tracks from 2a were colored for their apparent 2D diffusion coefficient. Apparent 2D diffusion coefficients were calculated using single-step mean-square displacement. Color bar represents the range of diffusion coefficients. Scale bar = 2 μm.

C) Distribution of the apparent 2D diffusion coefficients for the ER (grey) and LD (orange) localized *SBP-LiveDrop* tracks recorded with HILO imaging. A two-sided Mann-Whitney U-test was performed to compare ER and LD values. p = 3.1e-158.

D) Distribution of the anomalous diffusion exponent α for the ER (grey) and LD (orange) tracks recorded with HILO imaging**.** α was calculated by fitting a power law equation on the MSD curves. A two-sided Mann-Whitney U-test was performed for ER and LD tracks. p = 7e-259.

E) Types of motion signatures identified by DeepSPT. *SBP-LiveDrop* single-molecule tracks were clustered under four major categories: free-only motion (blue), confined-only motion (orange), single-motion switch (free-to-confined or confined-to-free), and tracks that switch between the two motion states multiple times.

F) Distribution of anomalous diffusion exponent α for free (blue) and confined (orange) tracks. Mann-Whitney U-test was performed for free and confined α values. p = 4.37e-167.

G) Distributions of apparent 2D diffusion coefficient for free (blue) and confined (orange) tracks. Mann-Whitney U-test was performed to compare free and confined populations. p = 6.44e-251.

H) *SBP-LiveDrop* single-molecule tracks from 3A were colored, based on motion state. Most ER localized tracks display free (blue) motion, but tracks that colocalize with LD marker (BODIPY-green) predominantly are confined. Scale bar = 2 μm.

I) Fractions of different motion states for ER and LD localized *SBP-LiveDrop* single-molecule tracks.

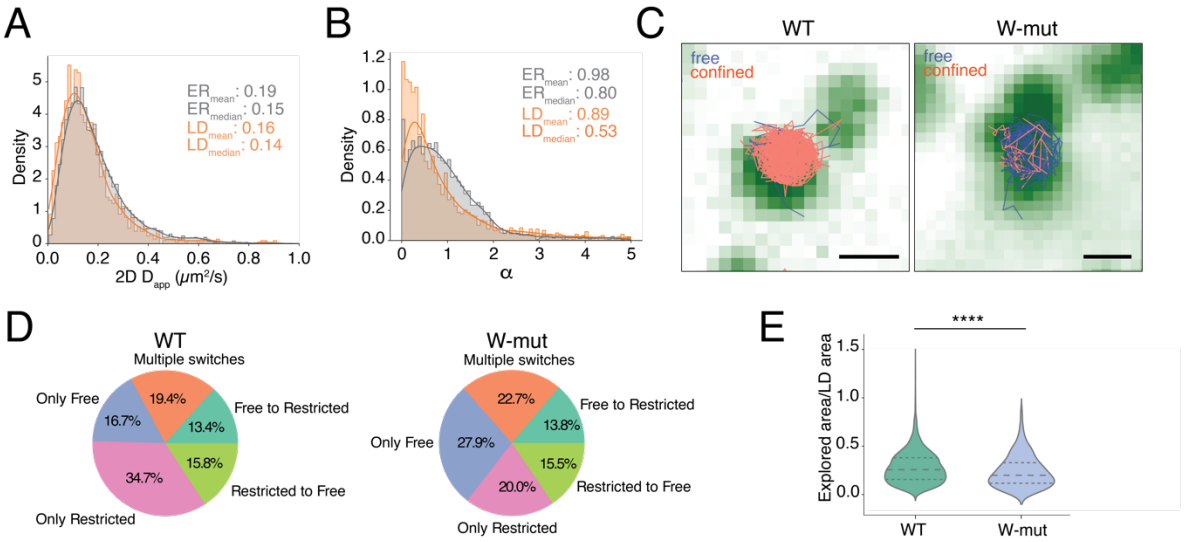

Figure 4. Tryptophan residues within the hairpin motif drive confinement on LDs

A) Distribution of the apparent 2D diffusion coefficients for the ER (grey) and LD (orange) localized W-mut tracks recorded with HILO imaging. A two-sided Mann-Whitney U-test was performed to compare ER and LD values. p = 2.2e-18.

B) Distribution of the α exponent for the ER (grey) and LD (orange) localized W-mut tracks recorded with HILO imaging. A two-sided Mann-Whitney U-test was performed to compare ER and LD values. p = 3e-23.

C) Motion states of single-molecule tracks for WT *SBP-LiveDrop and* W-mut overlaid on top of the LD channel. Scale bar: 500 nm.

D) Fractions of motion states observed on LDs from single-molecule tracks of WT and W-mut.

E) Areas explored for each single-molecule track within the corresponding BODIPY masks were plotted in a violin plot. A two-sided Mann-Whitney U-test was used to compare WT and W-mut values. p = 9.75e-5.

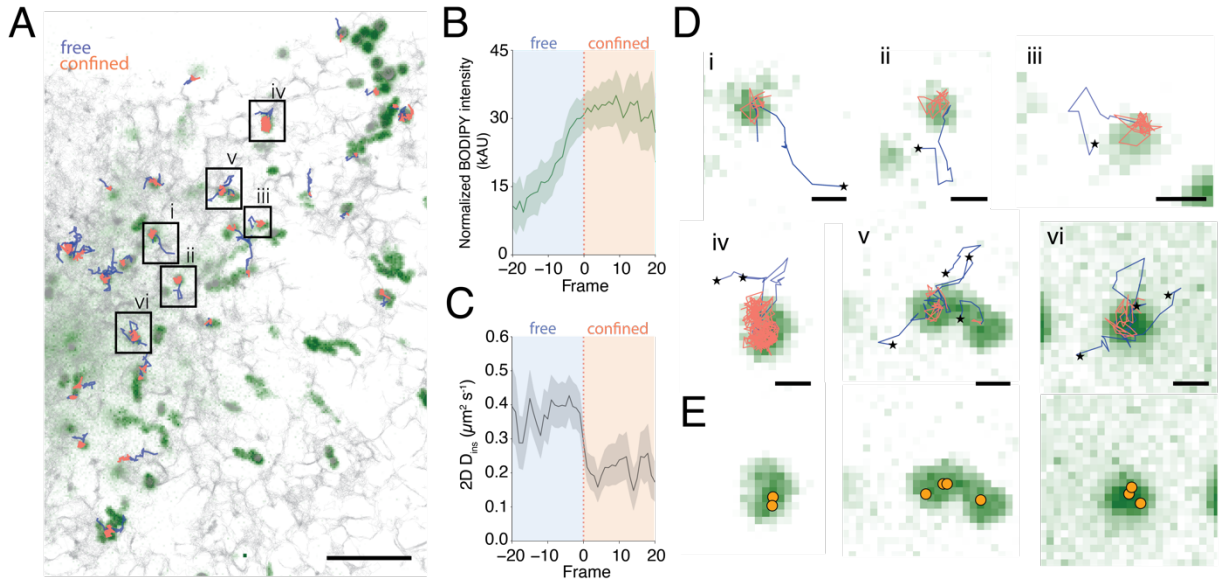

Figure 5. Protein entry to LD surface through ER-LD contact sites

A) ER-to-LD single-molecule tracks of SBP-*LiveDrop* 8 min post-biotin. Cells were treated with 250 µM oleic acid for 3 h prior to biotin release and labeled with 80 pM JFX554 prior to HILO imaging. Tracks switch from free (blue) to confined (orange) motion state upon travelling from the ER membrane to LD surface. All recorded tracks were colored as light grey. LDs were labelled with BODIPY 493/503 (green). Scale bar: 10 µm.

B) Mean BODIPY signal intensity along the ER-to-LD tracks are plotted with standard deviation. Free-to-confined switch is shown as Frame 0. An increase in BODIPY signal in the following frames indicates LD entry. n = 219 tracks.

C) Apparent 2D diffusion coefficient decreases after free-to-confined switch. A 100-ms rolling window means of diffusion coefficients along each ER-to-LD travelling tracks were calculated and plotted before and after the free-to-confined switch. A Mann-Whittney U-test was performed to compare values before and after the motion switch. p = 2.46e-105.

D) Examples of ER-to-LD travelling *SBP-LiveDrop* single-molecule tracks from Figure 4A. Tracks were colored, based on the motion state (blue = free, orange = confined). Track start points are indicated with a star. Scale bar: 500 nm.

E) The coordinates of free-to-confined motions switch of tracks from Figure 4E are plotted over LD channel (green).

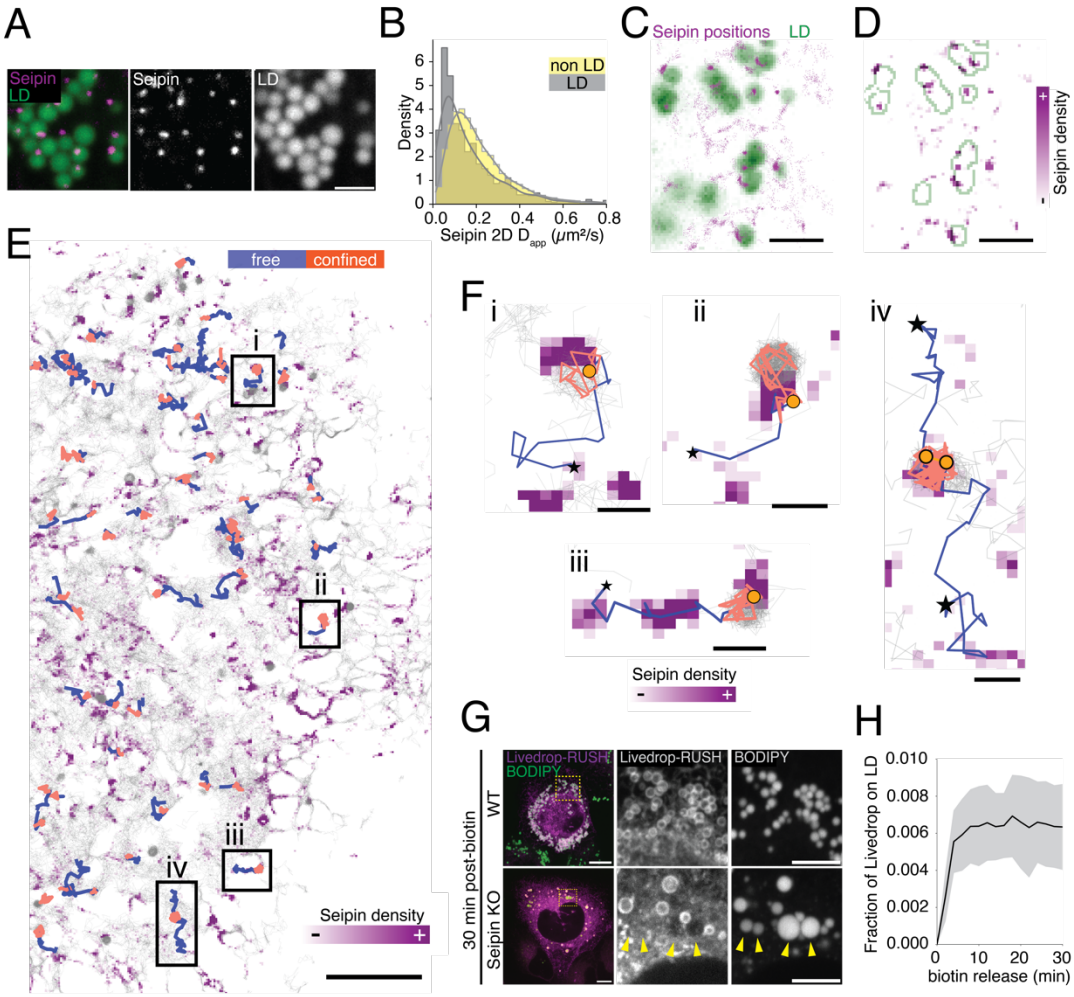

Figure 6. *SBP-LiveDrop* accesses LDs via seipin-containing ER-LD contact sites

A) Representative confocal images of endogenous tagged Seipin-sfGFP. Cells were incubated with 250 μM oleic acid overnight, labeled with LipidTOX Deep Red Lipid stain, and imaged under a spinning disk confocal microscope. Scale bar: 2 μm.

B) Apparent 2D diffusion coefficients of LD bound and free Seipin. Endogenously tagged Seipin was imaged using HILO microscope, and diffusion coefficients were calculated using single-step MSD. A two-sided Mann-Whitney U-test was performed to compare free vs LD bound Seipin tracks. p = 1.15e-39.

C) Seipin positions for individual Seipin complex were plotted over the LD channel. More Seipin positions were recorded in areas near LDs. Scale bar: 2 μm.

D) Seipin positions from Figure 4C were converted into a positional density map to mark for ER-LD contact sites. Positional densities were calculated by measuring the frequency of Seipin signal for each pixel and plotted as a colormap. Darker magenta indicates a higher density of Seipin positions (25+ positions) within a given pixel. Scale bar: 2 μm

E) Single-molecule tracks of *SBP-LiveDrop* plotted on top of the Seipin density map. Sparsely labeled SBP-*LiveDrop* and endogenously tagged Seipin were imaged simultaneously under a HILO microscope. An LD prediction algorithm was used to identify tracks travelling from the ER

to LDs (see methods). Tracks were colored, based on motion state. All SBP-*LiveDrop* tracks were colored as light grey. Scale bar: 10 µm.

F) Examples of *SBP-LiveDrop* single-molecule tracks entering LDs through Seipin dense regions. Tracks were colored, based on motion state (blue: free; orange: confined). Stars represent track start points. Coordinates of free-to-confined switch were used as a proxy for LD entry (orange circles). Scale bar: 500 nm.

G) Representative confocal images of *SBP-LiveDrop* in WT and Seipin knockout cells. Cells were incubated with 250 µM oleic acid overnight, and imaged with a spinning disk confocal microscope after a 30-min biotin release. Some LDs (yellow arrowheads) did not receive SBP-*LiveDrop* from the ER in Seipin KO cells (lower panel), indicating loss of ER-LD membrane contact. LDs were stained with 1 µM BODIPY 493/503. Scale bars: 10 µm (left), 5 µm (right).

H) Quantification of *SBP-LiveDrop* targeting kinetics. LD targeting ratio was calculated similar to Figure 1C.

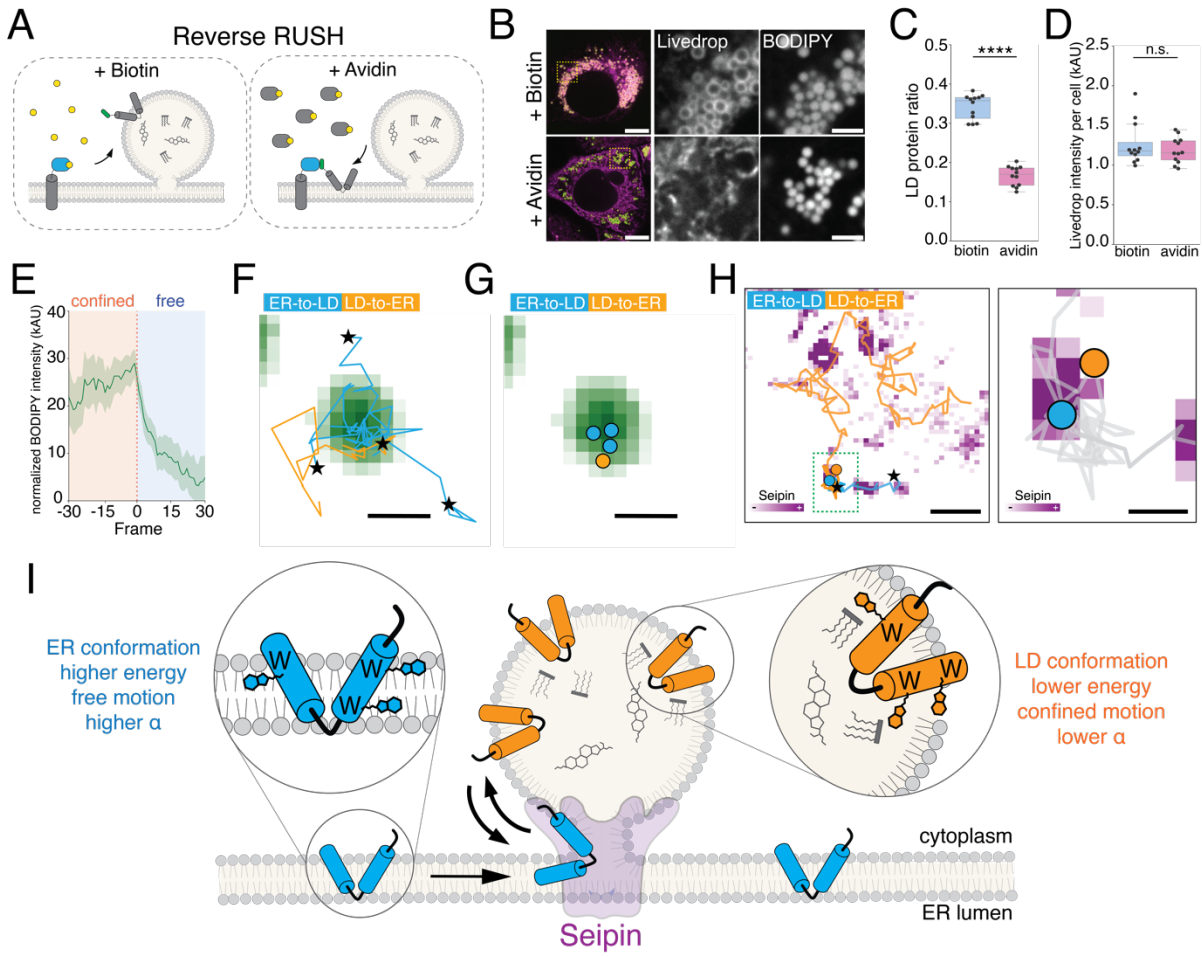

Figure 7. Protein movement across ER-LD contact sites is bidirectional

A) Schematic of "reverse RUSH" experiment. Cells were grown in biotin medium to allow SBP-*LiveDrop* to accumulate on LDs. Addition of avidin liberated the ER hook from biotin. Thus, any SBP-*LiveDrop* molecule that traveled back to the ER was captured and retained by the ER hook.

B) Representative confocal images of *SBP-LiveDrop* after overnight incubation with biotin (top) or avidin (bottom). Cells were incubated with biotin and oleic acid overnight to induce LD formation. LD-localized SBP-*LiveDrop* was labelled with 100 nM JFX554 prior to avidin addition. After overnight avidin treatment, cells were imaged with a confocal microscope. LDs were labelled with BODIPY (green). Scale bars: left:10 µm, right: 2 µm.

C) Quantification of *SBP-LiveDrop* targeting ratio, calculated similar to Figure 1C. A T-test was performed to compare biotin and avidin samples. p = 5.3e-10.

D) Quantification of total *SBP-LiveDrop* signal in cells. An unpaired t-test was performed to compare biotin and avidin samples. p = 0.86.

E) BODIPY signal intensity along single-molecule tracks that exited LDs. Confined-to-free switch is indicated as Frame 0. Mean values are shown with standard deviation. n = 331.

F) Representative *SBP-LiveDrop* single-molecule tracks travelling bidirectionally between the organelles. Tracks were recorded 8-minute post-biotin and analyzed using DeepSPT. Stars indicate track start points. Scale bar: 500 nm.

G) Coordinates of motion switch for ER-to-LD and LD-to-ER tracks from Figure 6F overlaid on LD channel. Scale bar: 500 nm.

H) Example of *SBP-LiveDrop* single-molecule tracks moving in both directions across a Seipin dense region near an LD. Coordinates of motion switch for both directions colocalized with a seipin density. Scale bars: 1 μm (left); 250 nm (right).

I) An “ER avoidance” model for LD protein targeting and accumulation. Hairpin containing proteins adopt free motion at the ER membrane and undergo confinement once they travel to LD surface through Seipin-mediated monolayer-bilayer membrane bridges. Confinement on LDs is driven by the bulky tryptophan residues (W) that favor packing defects within the LD surface over tightly packed ER membrane. This creates an energetical penalty at the ER membrane and drives LD targeting.